

Controlled Kinetics of On-Surface Dehydrogenation using a Low-Energy Electron Beam

Anton Makoveev

CEITEC – Central European Institute of Technology, Brno University of Technology, Purkyňova 123, 612 00 Brno

Pavel Procházka

Brno University of Technology <https://orcid.org/0000-0002-4727-4776>

Azin Shahsavar

Brno University of Technology

Lukáš Kormoš

<https://orcid.org/0000-0001-9099-4595>

Tomáš Krajňák

CEITEC - Central European Institute of Technology, Brno University of Technology, Purkyňova 123, 612 00 Brno

Veronika Stará

CEITEC - Central European Institute of Technology, Brno University of Technology, Purkyňova 123, 612 00 Brno

Jan Čechal (✉ cechal@fme.vutbr.cz)

CEITEC - Central European Institute of Technology, Brno University of Technology, Purkyňova 123, 612 00 Brno <https://orcid.org/0000-0003-4745-8441>

Article

Keywords: Self-Assembly, Low-Energy Electron Microscopy, Surfaces, Kinetics, On-Surface Reactions

Posted Date: December 21st, 2021

DOI: <https://doi.org/10.21203/rs.3.rs-1128962/v1>

License:  This work is licensed under a Creative Commons Attribution 4.0 International License.

[Read Full License](#)

Controlled Kinetics of On-Surface Dehydrogenation using a Low-Energy Electron Beam

Anton Makoveev,¹ Pavel Procházka,¹ Azin Shamsavar,¹ Lukáš Kormoš,¹ Tomáš Krajňák,¹

Veronika Stará¹ and Jan Čechal^{1,2}*

¹CEITEC – Central European Institute of Technology, Brno University of Technology,
Purkyňova 123, 612 00 Brno, Czech Republic.

²Institute of Physical Engineering, Brno University of Technology, Technická 2896/2, 616 69
Brno, Czech Republic.

ABSTRACT

Self-assembly and on-surface synthesis are vital strategies used for fabricating surface-confined 1D or 2D supramolecular nanoarchitectures with atomic precision. In many systems, the resulting structure is determined by kinetics of processes involved, i.e., reaction rate, on-surface diffusion, nucleation, and growth, all of which are typically governed by temperature. However, other external factors have been only scarcely harnessed to control the on-surface chemical reaction kinetics and self-assembly. Here, we show that a low-energy electron beam can be used to steer chemical reaction kinetics and induce the growth of molecular phases unattainable by thermal annealing. The electron beam provides a well-controlled means of promoting the elementary reaction step, i.e., deprotonation of carboxyl groups. The reaction rate linearly increases with increasing electron beam energy beyond the threshold energy of 6 eV. Our results offer the novel prospect of controlling the self-assembly, enhancing the rate of reaction steps selectively, and thus altering the kinetic rate hierarchy.

KEYWORDS. Self-Assembly; Low-Energy Electron Microscopy; Surfaces; Kinetics; On-Surface Reactions

INTRODUCTION

Bottom-up approaches provide the possibility to synthesize nanoscale architectures with atomic precision, thus offering the extensive prospect of creating materials with finely tuned properties. Since the first studies on self-assembled monolayers (SAMs),¹⁻³ multiple two-dimensional supramolecular assemblies on surfaces have been introduced,⁴⁻⁷ and a significant step in the on-surface synthesis has followed.⁸⁻¹⁰ The desired functionality is implemented by carefully designing molecular precursors and selecting a proper substrate. Besides thermodynamics, which defines the equilibrium structure, the kinetics of the involved on-surface processes,¹¹ i.e., reaction rate, on-surface diffusion, nucleation, and growth, plays a crucial role. The self-assembled structure is often defined by a self-assembly pathway,¹²⁻¹⁴ rather than thermodynamic stability; metastable, thermodynamically inaccessible, self-assembled nanostructures can be obtained under kinetic control.^{14,15} Considering the kinetic rates, generally all the involved processes are thermally activated following the Boltzmann distribution and display a particular hierarchy of activation energies, as shown in Figure 1. With an increasing temperature, the rate of all the temperature-activated processes increases exponentially, with activation energies being the defining parameter. The correct choice of temperature enables the adjustment of the rate of structural and chemical transformations to reach the desired product.^{10,16-19} However, this approach lacks spatial localization and does not selectively promote specific reaction steps because the hierarchy of activation energies cannot be easily rearranged.

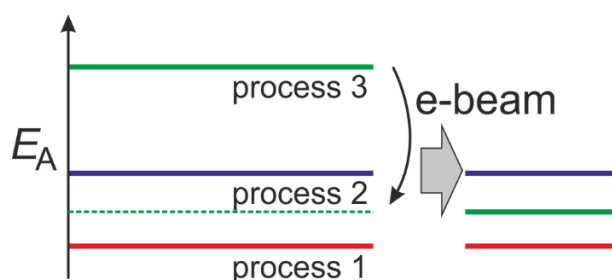


Figure 1: Schematic representation of a ladder of activation energies for three processes in a complex reaction. Considering the thermal activation, process 3 with the highest activation energy is rate-limiting. The e-beam irradiation selectively enables process 3; hence, with e-beam irradiation, process 2 becomes rate-limiting.

The non-thermal activation methods¹⁰ present an alternative that circumvents the limitations mentioned above. The activation induced by a scanning tunneling microscope (STM) tip provides ultimate control over the reaction kinetics, selectivity, and spatial localization^{20–23} but applies only to single-molecule modifications, preventing large-scale use and making it technologically irrelevant. Conversely, light and electron-beam (e-beam) probes generally encompass larger working areas and can excite specific vibrational modes, access many reaction channels, deliver much higher energies, and excite plasmons for plasmon-induced chemical reactions.^{10,24–29} E-beam-induced reactions like crosslinking/breaking polymer chains in electron beam lithography³⁰ or precursor decomposition in electron-beam-induced deposition (EBID)³¹ are key technologies for nanofabrication. Despite the advantages mentioned above, the irradiation methods have drawbacks; in particular, the utilization of light makes spatial localization diffraction limited. The commonly used high-energy e-beams deliver too high energy densities, causing extensive damage to adsorbed molecular layers, which substantially reduces reaction selectivity.²⁴ Even low-energy (< 20 eV) electrons are still considered rather more damaging than useful, especially for organic

adsorbates.²⁴ The interaction of low-energy (< 20 eV) electrons with organic molecules is associated, e.g., with radiation damage of biomolecules (e.g., DNA), degradation of materials, astrochemistry relevant reactions, polymerization in the condensed phase, and formation of reactive molecules and fragments in plasmas.^{32,33} With respect to on-surface synthesis and self-assembly, low-energy electrons have been employed so far to modify solution-processed carboxylic acid SAMs³⁴, induce polymerization of boronic acid on a Ag(001) surface interpreted as partial desorption of precursors providing free space for a reaction.³⁵ Indirectly, the e-beam-induced surface reconstruction pushed down the temperature of surface-assisted polymerization of alkanes by 20 K.³⁶ However, achieving reaction specificity and precise control of the reaction kinetics is still challenging. Here we show that a low-energy-electron beam provides excellent control over the kinetics of the dehydrogenation reaction and induces the growth of self-assembled molecular phases unattainable by conventionally used thermal annealing.

In this work, we use 4,4'-biphenyl-dicarboxylic acid (BDA, Figure 2a) to build initial supramolecular phases on Ag(001) and Ag(111) surfaces (Figures 2b, c). The carboxyl groups form stable complementary hydrogen-bonded synthons, thus being excellent building blocks to create self-assembled molecular architectures.^{7,37} Moreover, carboxylic acids play a prominent role in metal-coordinated^{38,39} and covalent coupling⁴⁰⁻⁴² on surfaces. We employ low-energy electron microscopy (LEEM) both as a source of low-energy electrons to induce chemical reactions and as a tool to measure their kinetics as a function of primary electron energy. To get a comprehensive picture of electron-induced chemical transformation, LEEM is complemented by STM, X-ray photoelectron spectroscopy (XPS), low-energy electron diffraction (LEED), and density-functional theory (DFT) calculations. Our results present novel prospects for driving self-assembly with high selectivity and spatial resolution.

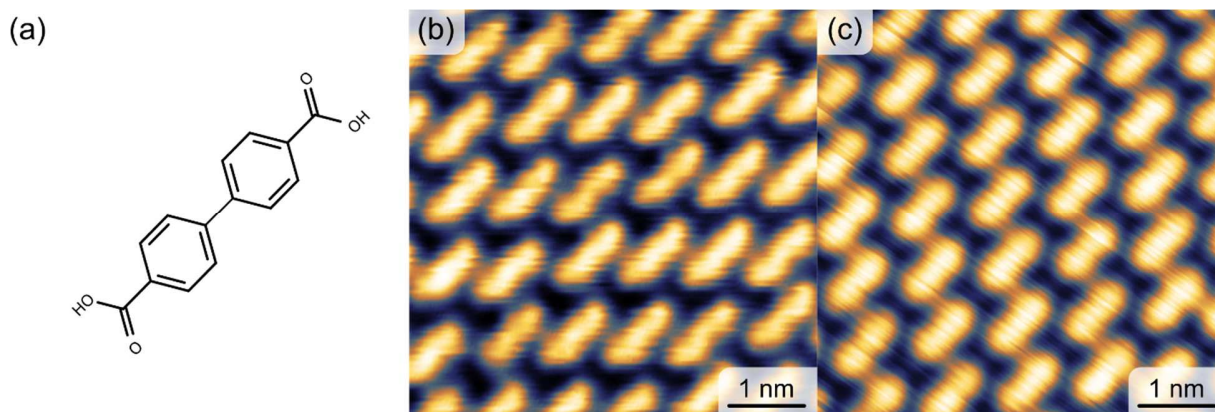


Figure 2. (a) Chemical structure of 4,4' biphenyl dicarboxylic acid (BDA). (b, c) STM images of the BDA α phases on (b) Ag(001) and (c) Ag(111) surfaces.

Results and Discussion

The as-deposited α phase (Figure 2b,c; and the corresponding diffraction pattern shown in Figure 3a) comprises an ordered network of hydrogen-bonded BDA molecules on both Ag(001)^{11,43,44} and Ag(111) substrates. The e-beam irradiation leads to the formation of new molecular phases. Depending on the electron energy, we distinguish two situations for the Ag(001) substrate. The sequence of LEED patterns presented in Figure 3b reveals that an e-beam with an energy lower than 10 eV first induces the formation of the intermediate β phase,¹¹ the structure of which is shown in Figure 3f. This is followed by further transformation to a molecular phase not observed in earlier works^{11,43,44} (denoted as the ε phase in the following). The structure of the ε phase is shown in Figure 3g). These transformations are a response to the chemical transformation of BDA, i.e., dehydrogenation (or deprotonation) of the carboxyl groups.¹¹ The β phase comprises 50 % of deprotonated groups,¹¹ and the ε phase is fully deprotonated (see Supporting Information, Section 1 for a detailed description of the ε phase). Whereas the formation of the β phase can be induced both by irradiation and thermal annealing above 340 K, the ε phase is only reached by e-beam irradiation. If the full deprotonation is reached thermally (>400 K), a distinct molecular phase (δ

phase) is formed instead.⁴⁴ The e-beam with an energy higher than 10 eV directly induces the formation of the ϵ phase, as documented in Figure 3c. This hints at a change in deprotonation- or growth kinetics when e-beam of a higher energy is used.

The e-beam deprotonation is also observed on the other silver substrate, Ag(111). On the Ag(111), the fully deprotonated phase (see Supporting Information, Section 2, for a description) is formed upon irradiation directly without any intermediate phase for all employed energies. This makes the quantification of the nucleation and growth rate straightforward for all the employed energies. In Supporting Information, Section 3, we show that the experiments performed at Ag(001) demonstrate qualitatively the same results if the ϵ phase grows directly. Figure 4 shows the evolution of the intensity of the diffraction spots associated with the fully deprotonated phase on Ag(001). Our data show that the higher the electron beam energy, the earlier the phase appears (black marks) and the faster it grows.

The formation of a new phase inherently relies on three physical processes: dehydrogenation (deprotonation) of the carboxylic groups, on surface transport and nucleation of deprotonated molecules, and subsequent growth of the phase itself, which, in turn, is defined by attachment and detachment of the constituents to the formed nuclei. The nucleation and growth of a new phase require supersaturation and a steady supply of its components, respectively. Hence, the shorter time needed for the nucleation of a new phase and its faster growth at higher energies suggests that the rate of BDA deprotonation increases with an increasing e-beam energy. However, these diffraction measurements include all three processes merged, making it challenging to prove that the e-beam influences only the deprotonation rate. Moreover, we have observed a slightly higher nucleation rate at an elevated temperature, as shown in the inset in Figure 4, which also complicates the unambiguous determination of the deprotonation rate independently on nucleation and growth.

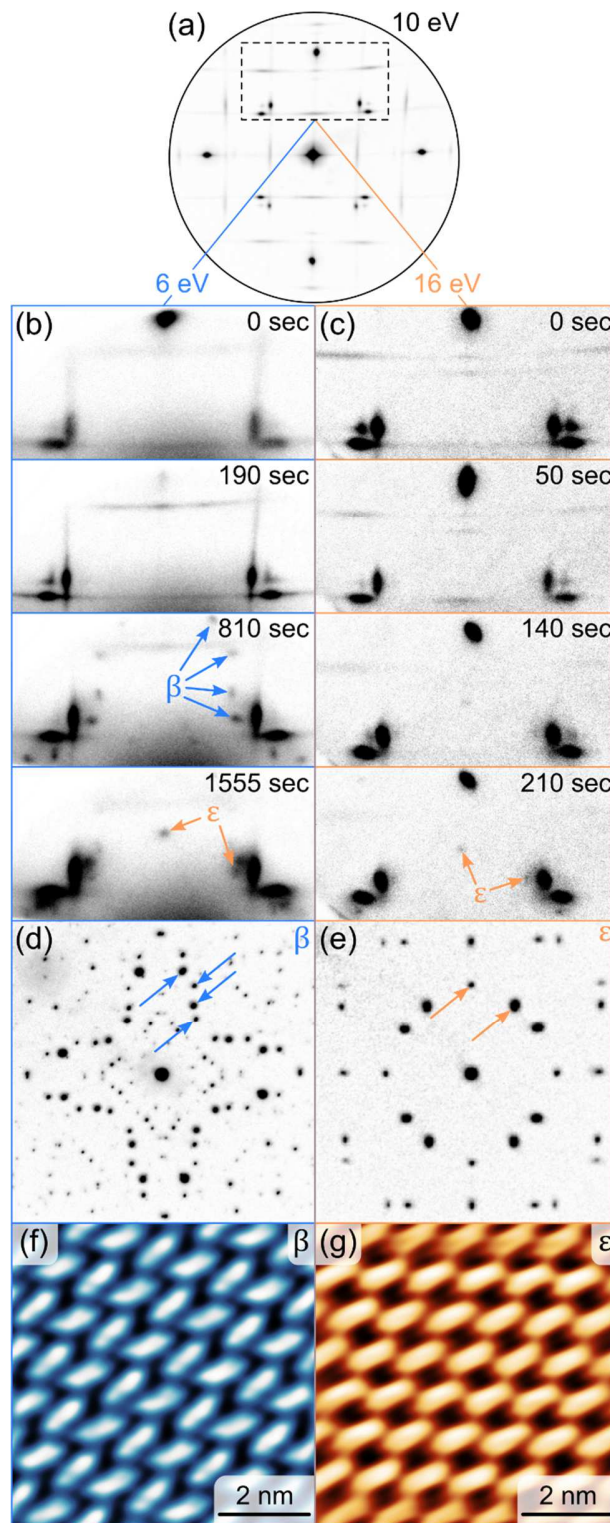


Figure 3. Phase evolution during e-beam irradiation. (a) Diffraction pattern of the initial α phase. (b, c) Diffraction-pattern sequences measured during e-beam irradiation at 6 eV (b) and 16 eV (c),

respectively. (d, e) The reference diffraction patterns of pure β phase (d) and ε phase (e). The arrows mark the positions of characteristic diffraction spots for each of the phases. (f, g) STM images of the β (f) and ε (g) phases.

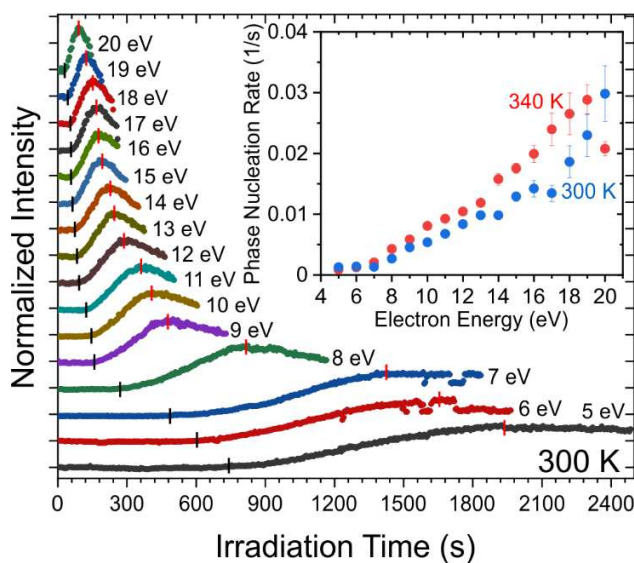


Figure 4. Time evolution of the intensity of diffraction spots associated with the fully deprotonated phase on Ag (111) for the energy of incident electron beam 5 – 20 eV. The black and red vertical lines mark the phase nucleation and maximum of the spot intensity, respectively. The inset summarizes the nucleation rate (inverse time necessary to nucleate the fully deprotonated phase) as a function of e-beam energy for temperatures 300 and 340 K.

Therefore, the measurements of the e-beam effect on the sample independent of nucleation and growth would be highly desirable. Recently, we have shown⁴³ that the temperature-induced transformation of the BDA α phase that form full layer on the Ag(001) surface fulfills this

condition. For a full monolayer coverage, the phase transformation proceeds differently than for submonolayer coverages: instead of the β phase, the so-called α phase is formed.⁴³ The transformation to the α phase proceeds internally and features the formation of a carboxylate-substrate bond, which requires only minor vertical and horizontal shifts of BDA within the existing structure. We found that similar transformation occurs within the BDA islands upon their e-beam irradiation. There are two possibilities for determining the deprotonation kinetics: the change in the intensity of diffraction spots associated with the α phase, and the change in the reflected electron beam intensity (further referred to as intensity) of BDA islands in the bright field images presented in Figure 5.

First, we consider the intensity of the diffraction spots associated with the α phase, marked by the red arrows in Figures 5e, f. The intensity of these spots gradually increases upon the e-beam irradiation and reaches the maximum at a certain point, beyond which the growing fraction of deprotonated carboxyl groups start to induce instabilities in the molecular phase, e.g., by deprotonation of the second carboxyl within a previously formed carboxyl-carboxylate synthon. These instabilities cause the rearrangement of BDA and lead to the decrease of intensity of diffraction spots associated with the α phase. We have determined the deprotonation rate as the inverse time from the beginning of the irradiation until the intensity of diffraction spots reaches its maximum (see Supporting Information, Section 4 for details). The results are given in Figure 5g: the growth rate of the α phase linearly increases with an e-beam energy above the energy of 6 eV. The presence of the low-energy offset and linear increase in deprotonation rate with the e-beam energy is consistent with the rates obtained from the nucleation of the fully deprotonated phase given in Figure 4.

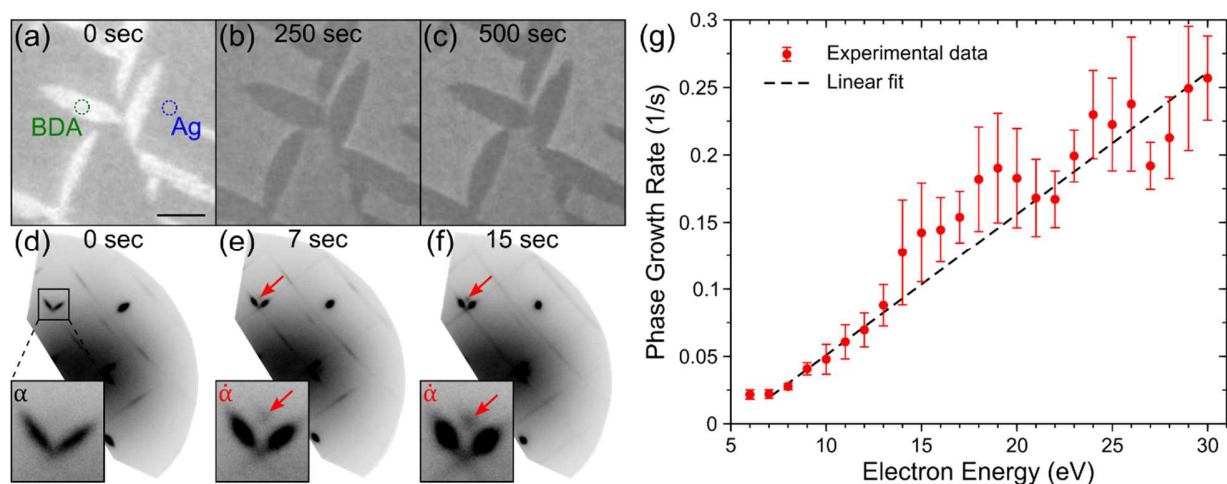


Figure 5. Changes in the bright-field images and diffraction patterns during irradiation by 12 eV e-beam. The upper series of the images (a-c) depicts the time evolution of contrast in bright-field LEEM (the scalebar is 0.3 μm). The green and blue circles indicate adsorbed BDA molecular islands and the Ag(001) substrate, respectively. The lower series (d-f) represents the time-dependent formation and intensity change of the diffraction spots associated with the α phase marked by red arrows. The insets show an enlarged vicinity of the main α phase diffraction spots. (g) The inverse-time value taken at the time when the maximum intensity of the diffraction spots affiliated with the α phase is reached depending on different e-beam energies. The error bars indicate one standard deviation. The dashed line is a linear fit of the experimental data in the range from 7 to 30 eV (reduced $\chi^2 \approx 0.826$).

The experiments performed in real space could provide spatially resolved reaction rates and involve lower e-beam energies (down to 1 eV) compared to diffraction. We observe that the measured intensity of the molecular phase irradiated with the e-beam decreases with irradiation

time (cf. Figures 5a–c and see Supporting Information, Section 5 for details). During the $\alpha \rightarrow \dot{\alpha}$ transformation, a carboxylate-oxygen–surface bond is formed, and the BDA molecule is pulled closer to the substrate, which decreases work function by ~ 0.2 eV due to the formation of interface dipole and push-back effect (see DFT calculations, Supporting Information, Section 6). As the difference in work function is one of the contrast mechanisms in LEEM,^{45,46} the observed contrast could be, in principle, proportional to the BDA deprotonation. We have experimentally confirmed that the dependence between the observed intensity and fraction of deprotonated carboxyl groups is linear up to at least 22 % of deprotonated carboxyl groups (Supporting Information, Section 7). However, according to the experimental calibration, the intensity should increase with a fraction of deprotonated molecules, i.e., should be the opposite in respect to behavior observed during the irradiation. This contradiction points to a distinct mechanism of the contrast change, e.g., the defocus of an electron beam image⁴⁷ induced by the charging of the BDA layer. Hence, the resemblance of the deprotonation rate dependence derived from bright field imaging (Figure S5.2 in Supporting Information, Section 5) with those measured by diffraction for energies up to 10 eV is somewhat of a coincidence, because a different physical quantity than the density of deprotonated carboxyl groups is measured. Hence, further research is required for a deeper understanding of the exact relationship between reaction rate and the observed intensity.

Based on the experiments presented above, we conclude that the growth of either the β or ε phase, depending on e-beam energy, is a direct consequence of the increased deprotonation rate of BDA molecules. Depending on its competition/cooperation with the nucleation rate, either the intermediate β phase or directly the final ε phase is formed. Regulation of the deprotonation rate thus allows a change of the limiting factor from the rate of supply of the deprotonated molecules to nucleation of the molecular phase. Hence, we show that rearranging the ladder of activation

energies defining the deprotonation-nucleation-growth kinetics can be employed to obtain different products.

However, the deprotonation reaction is also composed of several steps, i.e., O-H bond dissociation, detachment of a H atom from the reaction site, its on-surface diffusion, and associative desorption. At room temperature (RT), the electron beam dissociation is the rate-limiting step, and the remaining processes are active. Lowering the temperature should thus allow one to address whether the hydrogen dissociation is thermally assisted or solely induced by the e-beam. We have employed the XPS both to induce and follow the reaction. X-ray irradiation excites a significant number of secondary electrons, which may cause the deprotonation of carboxyl groups.⁴⁸ Figure 6a documents a gradual increase in the fraction of deprotonated carboxyl groups during the irradiation of the complete BDA layer on the Ag(001) substrate. A component at 531 eV highlighted by dotted vertical line is associated with the carboxyl–carboxylate bonding within the α phase. This component increases in intensity with continuous X-ray irradiation. The ratio of the intensity of this component to the original one can be employed to determine the fraction of deprotonated carboxyl groups, as detailed in Supporting information, Section 8. The evolution in the fraction of the deprotonated groups measured at several temperatures is given in Figures 6b, c, and d. The thermal contribution to deprotonation is negligible: as shown in Figure 6b, when we irradiated the sample only for 10-minute intervals within each hour, ~8 % of carboxyl groups was deprotonated during the 30-hour experiment; the total irradiation time was 300 min. The same fraction of deprotonated molecules was observed after 300 minutes of continuous irradiation. Hence, the observed change is solely induced by X-ray irradiation.

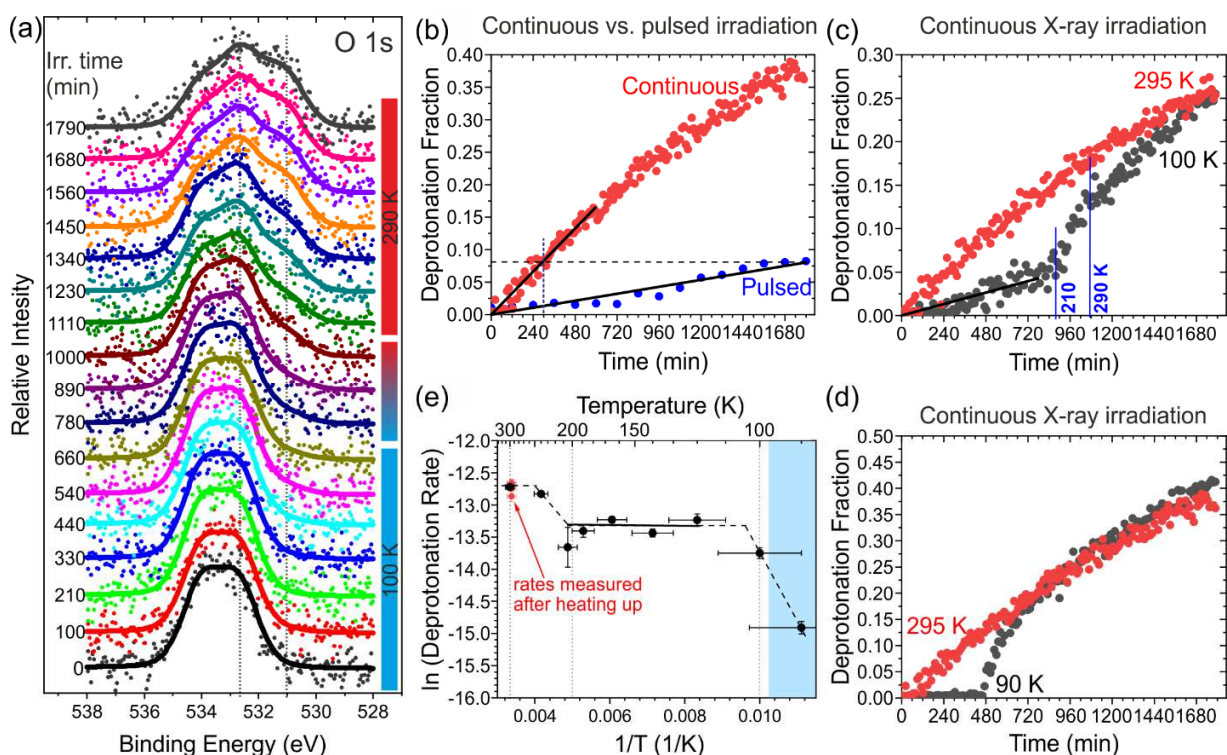


Figure 6. (a) Evolution of O 1s spectra during continuous X-ray irradiation at 100 K (marked by the cyan bar), during the heating-up, and finally at 290 K (red bar); irradiation time is given for each spectrum in minutes. Supporting information, Section 8 provides fitting of the spectra. (b) Evolution of the fraction of deprotonated carboxyl groups for continuous and pulsed (10 minutes in each hour) irradiation. (c, d) Evolution of the fraction of deprotonated carboxyl groups at 100 K (c) and 90 K (d) compared with room temperature (295 K). (e) Arrhenius-like plot showing the initial deprotonation rate (black); red points are the deprotonation rates measured at the same samples after sample heating to room temperature. We note that the deprotonation is faster for sub-monolayer coverages,⁴³ hence, the final deprotonation fraction is higher in Figure 6b and d (coverage ~ 0.95 ML) than Figure 6c (~ 1.05 ML).

The e-beam-induced deprotonation at lower temperatures, 90 and 100 K, is presented in Figures 6c and d. Irradiations below 200 K give two times lower deprotonation rates compared to the RT. However, when the sample is heated up to RT, the deprotonation rate first dramatically increases around 210 K (it is 2× higher than at RT) and then goes back to the RT value above 290 K. The final fraction of deprotonated carboxyl groups is the same regardless of the temperature history. The situation is even more pronounced at 90 K (Figure 6d); however, in this case, we observe the gradual increase of the O 1s signal probably associated with water adsorption⁴⁹ as shown in Supplementary Information, Section 9. The Arrhenius-like plot given in Figure 6e shows that the deprotonation rate is temperature independent between 100 – 200 K; the rate is significantly reduced due to water adsorption for lower temperatures. For temperatures above 200 K, the deprotonation rate reaches the RT value. Therefore, a significant change should occur around 200 K: there is an abrupt change in deprotonation rate both in the Arrhenius plot and during the heating up of the sample from low to RT during the continuous irradiation.

The rapid increase in deprotonation rate cannot be explained by the change in the rate of any associated process (i.e., O-H bond dissociation, detachment of H atom from reaction site, its on-surface diffusion, and associative desorption). The rates should be proportional to temperature but not to its derivative. We hypothesize that the hydrogen dissociation is induced by an electron beam and is temperature independent. Below 200 K, the hydrogen is not desorbed and remains near its parent carboxylate oxygen. As a result, the XPS spectra appear intact as no apparent change in the peak shape is visible. Above 200 K, the hydrogen desorption is thermally activated, and we observe pronounced changes in the O 1s spectra, as shown in Figure 6a. These changes can be associated with the rapid increase in the measured fraction deprotonated groups. In this respect, our DFT calculations detailed in Supporting Information, Section 10 show a stable intermediate state in

between the α and $\dot{\alpha}$ phases in which the dissociated hydrogen is bound to its parent carboxyl oxygen (Figure 7a). The activation barrier for leaving this position is ~ 0.6 eV, which fits the hydrogen associative desorption temperature above 200 K (the desorption rate at 200 K equals 10^{-3} s^{-1} taking the prefactor of 10^{13} s^{-1}). In summary, the XPS experiments show that an electron beam can exclusively control the O–H bond dissociation, whereas the rate of other reaction steps remains controlled by temperature.

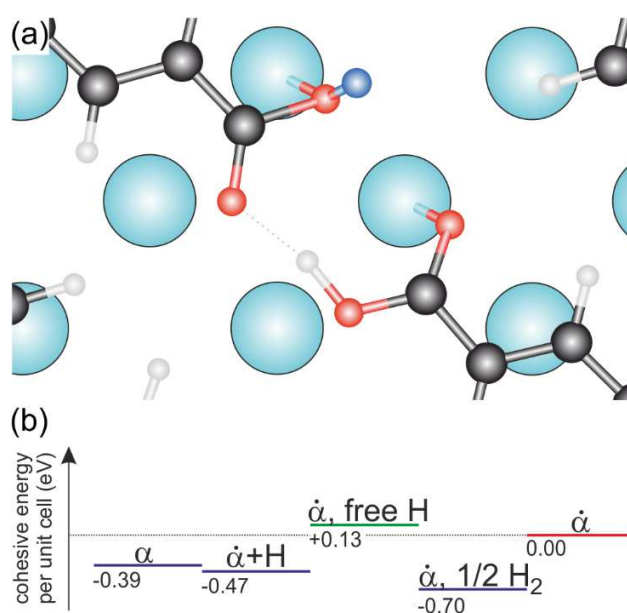


Figure 7. (a) DFT based model of the intermediate structure: an $\dot{\alpha}$ phase with H atom in the vicinity of its parent carboxyl oxygen (Ag: cyan, C: black, O: red, H: gray, the discussed H is blue). Full results are given in Supporting Information, Section 10. (b) Calculated enthalpies of several configurations referenced to the $\dot{\alpha}$ phase (marked $\dot{\alpha}$). α : α phase featuring the intact carboxyl group; $\dot{\alpha} + \text{H}$: $\dot{\alpha}$ phase with a hydrogen atom in the vicinity of its parent oxygen depicted in (a); $\dot{\alpha}, \text{ free H}$: $\dot{\alpha}$ phase with hydrogen atom artificially moved outside the surface, giving the maximum activation barrier (0.6 eV) for its diffusion out of the $\dot{\alpha} + \text{H}$ configuration. The corresponding

minimum barrier (0.5 eV) is given by the difference of $\dot{\alpha}$ and $\dot{\alpha}+H$ configurations. Finally, $\dot{\alpha}$, 1/2 H_2 , is associated with $\dot{\alpha}$ phase and the hydrogen in H_2 molecule in the gas phase.

Finally, we will discuss the possible mechanism of e-beam-induced deprotonation. The main interaction mechanisms of low-energy electrons with molecular samples are electron impact ionization (EII), electron impact excitation (EIE), and electron attachment (EA). The EII and EIE are non-resonant processes starting above the molecule's ionization potential (~ 10 eV) and above the excitation threshold (~ 6 eV), respectively, and gradually increasing with electron energy. In contrast, the EA is a resonant process typically occurring for electron energies below ~ 15 eV.³² The electron-stimulated desorption (ESD) experiments^{48,50,51} show a maximum hydrogen desorption rate from condensed carboxyl-containing organic molecules in the 10 – 15 eV range, which was assigned to the EA resonant process. For acetic acid, the O-H bonds were cleaved selectively over C-H bonds, and for electron energies < 15 eV, H is dissociated exclusively, i.e., no decarboxylation was observed.⁵¹ Contrary to these studies performed on molecular multilayers, we do not see any clear and ambiguous signatures of these, probably due to the proximity of the metallic substrate. Hence, we associate the monotonic increase of the reaction rate above 6 eV with the non-resonant electron impact excitation (EIE) process.

In our experiments, we cannot exclude other reaction pathways or the formation of by-products, e.g., decarboxylation. However, the formation of long-range ordered phases resulting from the e-beam irradiation suggests their low density, at least for employed electron doses, consistent with ESD studies.⁵¹ Future work should address the missing questions regarding the dissociation mechanism and the role of secondary electrons and plasmon excitations in on-surface reactions.

Another important piece of missing knowledge is to address the role of the substrate, i.e., the change in resonant energies for the dissociation of particular bonds and elucidate the presence or absence of quenching of electronic excitations occurring when molecules are electronically coupled with the metal substrate. With this knowledge, it would be possible to address individual reaction steps selectively and thus greatly enhance the control over on-surface synthesis and obtain new compounds not achievable otherwise.

DISCUSSION

In this work, we have investigated the transformation of BDA molecular phases on silver substrates induced by low-energy electrons at room temperature. Upon the irradiation by the primary electron beam, the BDA carboxyl groups deprotonate, leading to the growth of structurally different molecular phases. The deprotonation rate linearly increases with e-beam energy. Therefore, the electron energy can be used as a finely tunable tool to adjust the rate of the deprotonation reaction addressing only the dissociation step as revealed by XPS and DFT. Depending on the deprotonation rate, it is possible to form either the intermediate β phase for energies below 10 eV or the ϵ phase for higher energies. This demonstrates the principle of kinetic structural control, i.e., the formation of distinct periodic structures as a function of the external parameter.

Low-energy electron-beam irradiation is a promising reaction-activation tool for controlling self-assembly and chemical synthesis on surfaces, offering utilization of extensive knowledge gathered for electron-induced reactions,³² and the prospect for chemical lithography with nanometer-scale resolution.

Methods

The samples were prepared by the method described in refs. ^{11,43,44}. In brief, the experiments were performed in the UHV system at the CEITEC Nano Research Infrastructure. Samples were prepared and analyzed in separate chambers, between which samples can be transferred via a transfer line under UHV conditions (base pressure 2×10^{-10} mbar). BDA molecules (Sigma-Aldrich, 97% purity) were thermally deposited on Ag(001) and Ag (111) single crystals (MaTeck or SPL) that were cleaned by several cycles of Ar⁺ sputtering and annealing. Samples were analyzed by STM (Aarhus 150, Specs), LEEM/LEED (Specs FE-LEEM P90), and XPS (Phoibos 150, Specs).

LEEM. The transformation kinetics was followed in LEEM by measuring the evolution of bright-field images and diffraction patterns separately for a given set of energies. The bright-field kinetics was determined from video sequences (500 frames, 1sec/frame) recorded in real space at RT in a range of 2 – 30 eV with a step 2 eV. For each energy, the average intensity of the pristine BDA islands was measured in every frame and normalized to the average intensity of the pre-irradiated BDA islands. The data were collected from the small rectangular regions to eliminate the inhomogeneity of the background level.

XPS. XPS time series were acquired using non-monochromatized Mg K α radiation in normal emission geometry (emission angle 0 °). During the measurement, the sample was cooled by liquid N₂ flow to achieve the required temperature. Detailed O 1s spectra were acquired in a one-by-one sequence (medium magnification mode, 20 eV pass energy, acquisition time 10 min) during continuous sample irradiation by X-rays. After 500 – 800 minutes (depending on the experiment), we turned off the cooling, let the sample heat up to RT (300 – 400 min), and continued the measurements at RT with a total measurement time of ~1800 min. The spectra were fitted by Voigt

profiles after a Shirley or (Shirley + linear) background subtraction to determine the intensity ratios of the peak components.

Theory. Global energy minimizations were carried out using the density functional theory (DFT) approach by Vienna ab initio Simulation Package (VASP) as described in Supporting Information, Section 4.

ASSOCIATED CONTENT

Supporting information

The following files are available free of charge.

Description and further discussion of (1) Analysis of the ε phase on Ag(001), (2) The fully deprotonated phase on Ag(111), (3) Diffraction analysis of e-beam induced transformation at Ag(0001), (4) Reaction rate from the α to α' phase transformation, (5) Intensity change in the bright field as a function of electron energy, (6) DFT calculations: work function change upon deprotonation, (7) Electron reflectivity as a function of deprotonation fraction, (8) Details of fitting of the XPS data, (9) Water adsorption at 90 K, (10) DFT calculations: O-H dissociation (PDF)

AUTHOR INFORMATION

Corresponding Author

* E-mail: cechal@fme.vutbr.cz (J. Č.)

Author Contributions

The manuscript was written through the contributions of all authors.

AUTHOR CONTRIBUTIONS

A.M. prepared the samples, performed LEEM, STM, and XPS measurements, evaluated the LEEM/LEED data, and wrote the initial manuscript. P.P. designed LEEM/LEED experiments and performed the measurements. A.S. performed the DFT calculations. L.K., T.K., and V.S. prepared the samples and were involved in the analysis. J.Č. designed the experiment, evaluated XPS data, interpreted the results, and wrote the manuscript.

COMPETING INTERESTS

Authors declare no competing interests.

ACKNOWLEDGMENT

This research has been supported by GAČR, project No. 19-01536S. CzechNanoLab project LM2018110 funded by MEYS CR is gratefully acknowledged for the financial support of the measurements at CEITEC Nano Research Infrastructure. The theory part of this work was supported by the MEYS CR through the e-INFRA CZ (ID:90140). A.S. was supported by the ESF under the project CZ.02.2.69/0.0/0.0/20_079/0017436. We thank Andrea Konečná for her critical reading of the manuscript and valuable comments.

REFERENCES

1. Sagiv, J. Organized Monolayers by Adsorption. 1. Formation and Structure of Oleophobic Mixed Monolayers on Solid Surfaces. *J. Am. Chem. Soc.* **102**, 92–98 (1980).
2. Nuzzo, R. G. & Allara, D. L. Adsorption of Bifunctional Organic Disulfides on Gold Surfaces. *J. Am. Chem. Soc.* **105**, 4481–4483 (1983).
3. Casalini, S., Bortolotti, C. A., Leonardi, F. & Biscarini, F. Self-assembled monolayers in organic electronics. *Chem. Soc. Rev.* **46**, 40–71 (2017).
4. Elemans, J. A. A. W., Lei, S. & De Feyter, S. Molecular and Supramolecular Networks on Surfaces : From Two-Dimensional Crystal Engineering to Reactivity. *Angew. Chem. Int. Ed.* **48**, 7298–7332 (2009).
5. Bouju, X., Mattioli, C., Franc, G., Pujol, A. & Gourdon, A. Bicomponent Supramolecular Architectures at the Vacuum-Solid Interface. *Chem. Rev.* **117**, 1407–1444 (2017).
6. Goronzy, D. P. *et al.* Supramolecular Assemblies on Surfaces: Nanopatterning, Functionality, and Reactivity. *ACS Nano* **12**, 7445–7481 (2018).
7. MacLeod, J. Design and construction of on-surface molecular nanoarchitectures: lessons and trends from trimesic acid and other small carboxylated building blocks. *J. Phys. D. Appl. Phys.* **53**, 043002 (2020).
8. Shen, Q., Gao, H. & Fuchs, H. Frontiers of on-surface synthesis : From principles to applications. *Nano Today* **13**, 77–96 (2017).
9. Wang, T. & Zhu, J. Confined on-surface organic synthesis: Strategies and mechanisms. *Surf. Sci. Rep.* **74**, 97–140 (2019).

10. Clair, S. & De Oteyza, D. G. Controlling a Chemical Coupling Reaction on a Surface: Tools and Strategies for On-Surface Synthesis. *Chem. Rev.* **119**, 4717–4776 (2019).
11. Procházka, P. *et al.* Multiscale Analysis of Phase Transformations in Self-Assembled Layers of 4,4'-Biphenyl Dicarboxylic Acid on the Ag(001) Surface. *ACS Nano* **14**, 7269–7279 (2020).
12. Fukui, T. *et al.* Control over differentiation of a metastable supramolecular assembly in one and two dimensions. *Nat. Chem.* **9**, 493–499 (2017).
13. Korevaar, P. A. *et al.* Pathway complexity in supramolecular polymerization. *Nature* **481**, 492–496 (2012).
14. Haxton, T. K. *et al.* Competing thermodynamic and dynamic factors select molecular assemblies on a gold surface. *Phys. Rev. Lett.* **111**, 1–5 (2013).
15. Brown, R. D., Corcelli, S. A. & Kandel, S. A. Structural Polymorphism as the Result of Kinetically Controlled Self-Assembly. *Acc. Chem. Res.* **51**, 465–474 (2018).
16. Wang, T. *et al.* Kinetic Strategies for the Formation of Graphyne Nanowires via Sonogashira Coupling on Ag(111). *J. Am. Chem. Soc.* **140**, 13421–13428 (2018).
17. Cirera, B. *et al.* Thermal selectivity of intermolecular versus intramolecular reactions on surfaces. *Nat. Commun.* **7**, 1–8 (2016).
18. Eichhorn, J. *et al.* On-surface ullmann coupling: The influence of kinetic reaction parameters on the morphology and quality of covalent networks. *ACS Nano* **8**, 7880–7889 (2014).

19. Gutzler, R., Cardenas, L. & Rosei, F. Kinetics and thermodynamics in surface-confined molecular self-assembly. *Chem. Sci.* **2**, 2290–2300 (2011).
20. Sloan, P. A. & Palmer, R. E. Two-electron dissociation of single molecules by atomic manipulation at room temperature. *Nature* **434**, 367–371 (2005).
21. Pavliček, N. *et al.* Polyynes formation via skeletal rearrangement induced by atomic manipulation. *Nat. Chem.* **10**, 853–858 (2018).
22. Auburger, P. *et al.* Microscopic Insight into Electron-Induced Dissociation of Aromatic Molecules on Ice. *Phys. Rev. Lett.* **121**, 206001 (2018).
23. Heintz, J., Durand, C., Tang, H. & Coratger, R. Control of the deprotonation of terephthalic acid assemblies on Ag(111) studied by DFT calculations and low temperature scanning tunneling microscopy. *Phys. Chem. Chem. Phys.* **22**, 3173–3183 (2020).
24. White, J. M. Using photons and electrons to drive surface chemical reactions. *J. Mol. Catal. A Chem.* **131**, 71–90 (1998).
25. Urgel, J. I. *et al.* On-surface light-induced generation of higher acenes and elucidation of their open-shell character. *Nat. Commun.* **10**, 1–9 (2019).
26. Kazuma, E., Jung, J., Ueba, H., Trenary, M. & Kim, Y. Plasmon-induced chemical reaction of a single molecule. *Science (80-.)*. **526**, 521–526 (2018).
27. Zhou, L. *et al.* Response to Comment on “Quantifying hot carrier and thermal contributions in plasmonic photocatalysis”. *Science (80-.)*. **364**, 69–72 (2019).
28. Yan, L., Wang, F. & Meng, S. Quantum Mode Selectivity of Plasmon-Induced Water

- Splitting on Gold Nanoparticles. *ACS Nano* **10**, 5452–5458 (2016).
29. Grossmann, L. *et al.* On-surface photopolymerization of two-dimensional polymers ordered on the mesoscale. *Nat. Chem.* **13**, 730–736 (2021).
 30. Chen, Y. Nanofabrication by electron beam lithography and its applications: A review. *Microelectron. Eng.* **135**, 57–72 (2015).
 31. Huth, M. *et al.* Focused electron beam induced deposition: A perspective. *Beilstein J. Nanotechnol.* **3**, 597–619 (2012).
 32. Arumainayagam, C. R., Lee, H. L., Nelson, R. B., Haines, D. R. & Gunawardane, R. P. Low-energy electron-induced reactions in condensed matter. *Surf. Sci. Rep.* **65**, 1–44 (2010).
 33. Böhler, E., Warneke, J. & Swiderek, P. Control of chemical reactions and synthesis by low-energy electrons. *Chem. Soc. Rev.* **42**, 9219–9231 (2013).
 34. Asyuda, A. *et al.* Electron-Induced Modification of Self-Assembled Monolayers of Aromatic Carboxylic Acids. *J. Phys. Chem. C* **124**, 25107–25120 (2020).
 35. Clair, S., Ourdjini, O., Abel, M. & Porte, L. Tip- or electron beam-induced surface polymerization. *Chem. Commun.* **47**, 8028–8030 (2011).
 36. Sun, K. *et al.* Surface-Assisted Alkane Polymerization: Investigation on Structure-Reactivity Relationship. *J. Am. Chem. Soc.* **140**, 4820–4825 (2018).
 37. Ivasenko, O. & Perepichka, D. F. Mastering fundamentals of supramolecular design with carboxylic acids. Common lessons from X-ray crystallography and scanning tunneling

- microscopy. *Chem. Soc. Rev.* **40**, 191–206 (2011).
38. Dong, L., Gao, Z. A. & Lin, N. Self-assembly of metal–organic coordination structures on surfaces. *Prog. Surf. Sci.* **91**, 101–135 (2016).
39. Cechal, J. *et al.* Convergent and divergent two-dimensional coordination networks formed through substrate-activated or quenched alkynyl ligation. *Chem. Commun.* **50**, 9973–9976 (2014).
40. Gao, H. Y. *et al.* Decarboxylative polymerization of 2,6-naphthalenedicarboxylic acid at surfaces. *J. Am. Chem. Soc.* **136**, 9658–9663 (2014).
41. Held, P. A. *et al.* On-Surface Domino Reactions: Glaser Coupling and Dehydrogenative Coupling of a Biscarboxylic Acid To Form Polymeric Bisacylperoxides. *Angew. Chemie - Int. Ed.* **55**, 9777–9782 (2016).
42. Lindner, R. & Kühnle, A. On-surface reactions. *ChemPhysChem* **16**, 1582–1592 (2015).
43. Procházka, P. *et al.* Phase transformations in a complete monolayer of 4,4'-biphenyl-dicarboxylic acid on Ag(0 0 1). *Appl. Surf. Sci.* **547**, (2021).
44. Kormoš, L., Procházka, P., Makoveev, A. O. & Čechal, J. Complex k-uniform tilings by a simple bitopic precursor self-assembled on Ag(001) surface. *Nat. Commun.* **11**, 1856 (2020).
45. Tromp, R. M. Low-energy electron microscopy. *IBM J. Res. Dev.* **44**, 503–516 (2000).
46. Prieto, M. J. & Schmidt, T. LEEM and PEEM as Probing Tools to Address Questions in Catalysis. *Catal. Letters* **147**, 2487–2497 (2017).

47. Nataf, G. F. *et al.* Low energy electron imaging of domains and domain walls in magnesium-doped lithium niobate. *Sci. Rep.* **6**, 33098 (2016).
48. Boudaïffa, B., Cloutier, P., Hunting, D., Huels, M. A. & Sanche, L. Resonant formation of DNA strand breaks by low-energy (3 to 20 eV) electrons. *Science (80-.)*. **287**, 1658–1660 (2000).
49. Henderson, M. The interaction of water with solid surfaces: fundamental aspects revisited. *Surf. Sci. Rep.* **46**, 1–308 (2002).
50. Sedlacko, T. *et al.* Reactions in condensed formic acid (HCOOH) induced by low energy (< 20 eV) electrons. *Phys. Chem. Chem. Phys.* **7**, 1277–1282 (2005).
51. Bertin, M. *et al.* Electron stimulated desorption of H⁻ ions from condensed acetic acid. *Chem. Phys. Lett.* **433**, 292–295 (2007).

Supplementary Files

This is a list of supplementary files associated with this preprint. Click to download.

- [MakoveevBDAebeamSI.pdf](#)